© 2020. Published by The Company of Biologists Ltd | Journal of Experimental Biology (2020) 223, jeb226654. doi:10.1242/jeb.226654

RESEARCH ARTICLE

Remoras pick where they stick on blue whales

Brooke E. Flammang[1,*], Simone Marras[2,3], Erik J. Anderson[4,5], Oriol Lehmkuhl[6], Abhishek Mukherjee[2], David E. Cade[7,8], Michael Beckert[9,10], Jason H. Nadler[9], Guillaume Houzeaux[6], Mariano Vázquez[6], Haley E. Amplo[1], John Calambokidis[11], Ari S. Friedlaender[8] and Jeremy A. Goldbogen[7]

ABSTRACT

Animal-borne video recordings from blue whales in the open ocean show that remoras preferentially adhere to specific regions on the surface of the whale. Using empirical and computational fluid dynamics analyses, we show that remora attachment was specific to regions of separating flow and wakes caused by surface features on the whale. Adhesion at these locations offers remoras drag reduction of up to 71–84% compared with the freestream. Remoras were observed to move freely along the surface of the whale using skimming and sliding behaviors. Skimming provided drag reduction as high as 50–72% at some locations for some remora sizes, but little to none was available in regions where few to no remoras were observed. Experimental work suggests that the Venturi effect may help remoras stay near the whale while skimming. Understanding the flow environment around a swimming blue whale will inform the placement of biosensor tags to increase attachment time for extended ecological monitoring.

KEY WORDS: Adhesion, Echeneidae, Biologging tag, Drag, Boundary layer

INTRODUCTION

There are considerable challenges to be overcome to find food and mates in the open ocean, particularly for smaller fishes that are non-migratory. In what may have evolved as a novel functional approach to mediate this (Gamel et al., 2019), remora fishes (family Echeneidae) adhere to the surface of other swimming organisms, including sharks, mantas, marlin, turtles, dolphins and whales, using a modified dorsal fin (Andrade, 2007; Brunnschweiler and Sazima, 2006; Fertl and Landry, 1999; Gudger, 1919; Kenaley et al., 2019; O'Toole, 2002). Their relationship is considered symbiotic, as many species of remoras feed on parasites on the host surface which would otherwise reduce host health (Cressey and Lachner, 1970; Strasburg, 1962), in return for bits of host prey, reduced locomotor cost and predation risk, and increased likelihood of meeting conspecifics (Muir et al., 1967; Silva-Jr and Sazima, 2003; Steffensen and Lomholt, 1983).

However, exactly why remoras select specific locations on a host's body is unknown. It has long been speculated that for any particular host organism, remoras may preferentially adhere to particular locations on the host body to lower host irritation, reduce drag or increase likelihood of food availability (Douglas and Calambokidis, 2001; Weihs et al., 2007). Unfortunately, remora location data are typically derived from single photographs, often at the sea surface for cetaceans, or from short observations of a host organism (Fig. 1). No studies have continuously followed the precise positions and movement patterns of remoras on a host for any period of time.

A unique opportunity to study remora position and behavior *in situ* became available through the development of biologging tags with video capabilities that are deployed on host species, including large baleen whales like blue whales (*Balaenoptera musculus*). Here, remoras were observed interacting with each other and moving along the whale in specific locations on the whale body. Their preference for specific attachment locations suggests that some physical and/or biotic conditions at those sites encourage remora adhesion. Hydrodynamic conditions, especially drag, would vary for remoras along the body of a large swimming organism, such as the blue whale.

Remora bodies are streamlined and are estimated to contribute a low 'parasitic drag' on hosts such as dolphins or sharks (Beckert et al., 2016a). However, drag experienced by the remora may be relatively high. Median blue whale swimming speed has been recorded at 2.1±0.5 m s^{-1} (7.6±1.8 km h^{-1}) and at 3.9±0.8 m s^{-1} (14±2.9 km h^{-1}) during rapid feeding bursts (Cade et al., 2016; Gough et al., 2019). Given that remoras can grow to 1 m (Lieske and Myers, 1994), riding a blue whale in those circumstances represents speeds of more than 2–4 body lengths (BL) s^{-1} for the remora. By contrast, most fishes are known to swim comfortably at around 1–2 BL s^{-1} and few can maintain speeds over 2 BL s^{-1} for an extended duration (Jayne and Lauder, 1996; Lauder, 2006). Although remora could potentially keep pace with a blue whale by burst swimming and resting during attachment, we hypothesized that their preferential localization on and swimming behaviors near a blue whale are, at least in part, related to the reduction of hydrodynamic drag and detachment forces, thus lowering energy use and reducing the likelihood of separation from the host. Here, we used high-performance computing and computational fluid dynamics to investigate the hydrodynamic environment around the body of a freely swimming blue whale including a case with remoras attached. We used the computational results and empirical data specific to streamlined bodies attached to surfaces (Hoerner, 1965) to determine drag on remoras and compare that information with the site specificity of remora attachment. Through this work, we hope to better our understanding of both the flow environments around an organism and the mechanisms by which specifically adapted

[1]Federated Department of Biological Sciences, New Jersey Institute of Technology, Newark, NJ 07102, USA. [2]Department of Mechanical & Industrial Engineering, New Jersey Institute of Technology, Newark, NJ 07102, USA. [3]Center for Applied Mathematics and Statistics, New Jersey Institute of Technology, Newark, NJ 07102, USA. [4]Department of Applied Ocean Physics and Engineering (Guest Investigator), Woods Hole Oceanographic Institution, Woods Hole, MA 02543, USA. [5]Department of Mechanical Engineering, Grove City College, Grove City, PA 16127, USA. [6]Department of Computer Applications in Science and Engineering, Barcelona Supercomputing Center, 08034 Barcelona, Spain. [7]Hopkins Marine Station, Department of Biology, Stanford University, Pacific Grove, CA 93950, USA. [8]Institute for Marine Sciences, University of California Santa Cruz, 15 McAllister Way, Santa Cruz, CA 95003, USA. [9]Advanced Concepts Research Laboratory, Georgia Tech Research Institute, Atlanta, GA 30332, USA. [10]Exponent Engineering and Scientific Consulting, 3350 Peachtree Road NE, Suite 1125, Atlanta, GA 30326, USA. [11]Cascadia Research Collective, Olympia, WA 98501, USA.

*Author for correspondence (flammang@njit.edu)

B.E.F., 0000-0003-0049-965X

Received 9 April 2020; Accepted 7 September 2020

Journal of Experimental Biology (2020) 223, jeb226654. doi:10.1242/jeb.226654

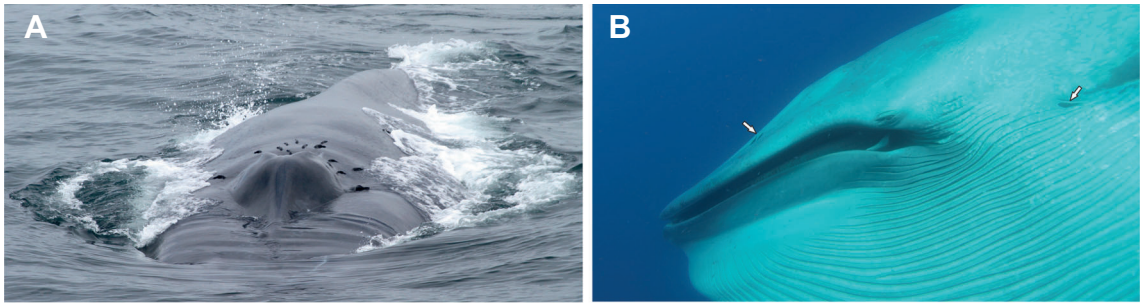

Fig. 1. Remora attachment sites as documented by photograph at the water surface and underwater video. (A) Remoras around the blowhole (photo credit: Todd Pusser, J.C.). (B) Underwater photo of a blue whale with remoras attached to the rostrum and axillary region (white arrows). Photo reproduced here with permission, filmed for the BBC television series 'The Hunt' (producer, Hugh Pearson; copyright Silverback Films/David Reichert, in collaboration with J.C.).

organisms like remoras successfully attach to hosts in order to improve animal tag technologies and designs for extended periods of behavioral and ecological monitoring.

MATERIALS AND METHODS

Specimens

Whales were tagged following Stanford University IACUC 30123 and NOAA Fisheries permit 16111 to J.C. Fishes used in experiments were handled humanely and ethically following New Jersey Institute of Technology/Rutgers University IACUC protocol 17058-A0-R1.

Tag data

Video footage of remoras attached to blue whales [*Balaenoptera musculus* (Linnaeus 1758)] was opportunistically recorded from suction cup-attached, multi-sensor video bio-logging tags from Customized Animal Tracking Solutions (CATS) (Cade et al., 2018; Goldbogen et al., 2017) used for ecological tracking studies on 6–20 August 2014 off of Palos Verdes and San Diego, CA, USA. The tag was 23 cm×13 cm×4.5 cm in size, 654 g in mass, and designed to stick to the whale body surface with four suction cups at its base. All tags were deployed from a 6 m rigid-hull inflatable boat using a 6 m pole. The tag housed dual cameras, each of which recorded video at 720×1280 pixels, at a variable frame rate of 22–24 frames s^{-1}. Accelerometers, magnetometers and gyroscopes were sampled at 40 Hz, and pressure, light, temperature and GPS at 10 Hz. Data were decimated to 10 Hz, tag orientation on the animal was corrected for, and animal orientation was calculated using custom-written MATLAB scripts (Cade et al., 2016; Johnson and Tyack, 2003). Animal speed for all deployments was determined using the amplitude of tag vibrations (Cade et al., 2018). Tag position and orientation were confirmed through observation during tracking sequences, through heading, pitch and roll calculations from tag positional sensor output, and through orientation to the whale body in videos. Using recorded data from the CATS multi-sensor camera tags, we were able to visually identify each remora's position on the whale body (Fig. 2), including its attachment relative to the blue whale's rostrum, x (m), and the velocity of the whale U_0 (m s^{-1}).

We had the opportunity to augment the CATS tag dataset using underwater video to confirm whether remoras selected different positions on the whale body in the absence of the tag and found no difference in attachment location. Underwater video was filmed as a part of scientific research under permit off the coast of southern California for the BBC television series 'The Hunt' produced by Hugh Pearson, in collaboration with J.C. (Fig. 1B). All procedures were conducted under approval of the National Marine Fisheries Service (permits 16111, 19116, 15271); National Marine Sanctuaries (MULTI-2017-007); and institutional IACUC committees.

To test for site specificity on the body surface of the blue whale, a Rayleigh distribution test for non-uniformity was used. If we consider the blue whale surface to be uniformly equal in terms of non-specificity of attachment environment at any location, we can test for non-random concentrations of remora positions using the Rayleigh distribution test (Brazier, 1994).

Computational fluid dynamics (CFD) analysis

Design of the numerical simulations

The finite element-based numerical solver Alya (Vázquez et al., 2016) was utilized to solve the Navier–Stokes equations of turbulent incompressible flows. Turbulence was handled by means of a large eddy simulation (LES) model whose details are given below. Equal-order finite elements (equal order interpolation of velocity and pressure) were used, and pressure was stabilized via a non-incremental fractional-step method (Charnyi et al., 2017; Lehmkuhl et al., 2019). This approach was demonstrated to conserve linear and angular momentum at the discrete level. The equations are solved forward in time to reach a steady-state by means of an energy-conserving explicit Runge–Kutta method (Capuano et al., 2017) with adaptive time stepping. The adaptive time-step procedure relies on the analytical bounding of the eigenvalues of the dynamical system to adapt the linear stability domain of the Runge–Kutta scheme for time-step maximization (Trias and Lehmkuhl, 2011).

The whale geometry was obtained from a three-dimensional scan of a commissioned scale replica at 1:100 size. The digital stereolithography file was then imported into the numerical mesh generator to build a mesh. Based on underwater observations, an average whale speed of U_0=1.5 m s^{-1} was estimated. This free-stream velocity of water with kinematic viscosity $\nu=1.3\times10^{-6}$ m^2 s^{-1} and a whale length c=18 m yield a Reynolds number $Re_c\approx22.7\times10^6$. The computational domain is a parallelepiped 9 whale lengths long in the stream-wise direction, 25 average whale diameters in the span-wise direction, and 20 average whale diameters in the vertical direction.

A set of two simulations was performed using two meshes of increasing resolution. The first one was a spin-up simulation based on a relatively coarse-grained mesh, or 'grid' (approximately 27 million finite elements; Fig. 3) to estimate the necessary time for a steady-state solution to be reached given the available computational resources. The steady state was reached in 8 h of wall-clock time using 720 cores of MareNostrum IV at the Barcelona Supercomputing Center. The steady-state solution was then interpolated onto the fine-resolution mesh of 42 million

Journal of Experimental Biology (2020) 223, jeb226654. doi:10.1242/jeb.226654

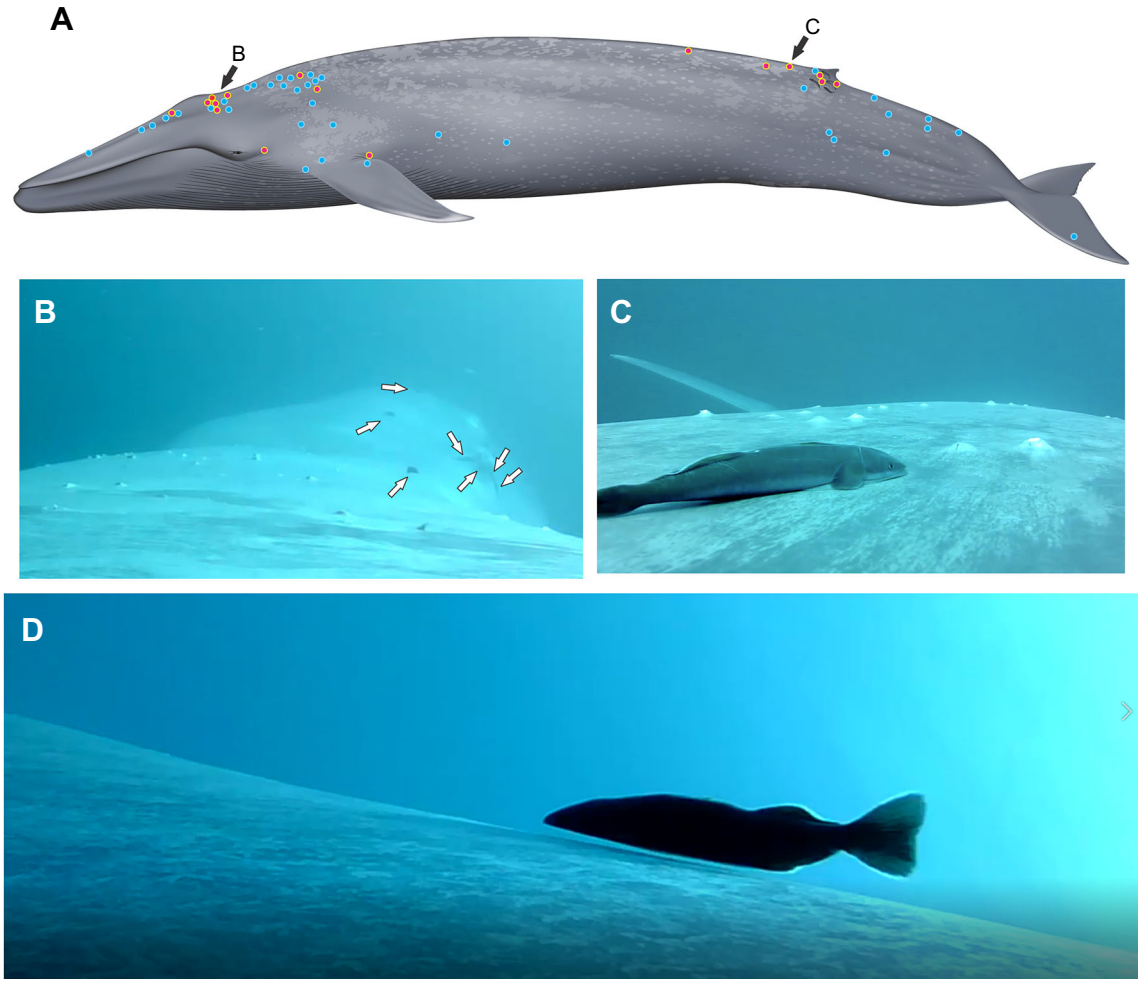

Fig. 2. Remora attachment locations on a 26 m blue whale as observed by continuous recording via CATS camera tag. (A) Blue circles indicate the position where at least one remora was observed; the red circles with yellow outline indicate high-density sites (greater than 3 remoras at a time). Whale image credit: NOAA Fisheries. (B) Remoras attached near the blowhole (each white arrow points to a remora). (C) *Remora australis* positioned near the dorsal fin. (D) Remora skimming while moving to a more anterolateral position on the whale.

elements as the initial state for the high-resolution simulation whose results are discussed in this article. By doing this, 6000 core hours were saved for the 42 million simulation compared with the case of an initially uniform velocity field. At an advective Courant number of 1, the high-resolution simulation was executed for 48 h of wall-clock time using as many computing cores as for the 27 million simulation.

The spin-up solution was also used to obtain an estimation of the boundary layer thickness and hence inform the construction of a proper boundary layer grid (Fig. 3B) for the 42 million simulation. Although the two meshes contain a comparable number of elements, the 42 million simulation mesh was designed by refining the element distribution in those regions where important flow gradients were measured in the spin-up simulation. Informed by the boundary layer thickness measured in the spin-up test, the boundary layer mesh of the 42 million simulation mesh was designed to fully contain the boundary layer. It was made of 8 vertical prismatic levels with a triangular base and varying thickness from 1.26 mm in the first layer to 0.36 mm in the eighth layer. With a total of 5.5 million prisms, this boundary layer grid represents 13% of the total element count. The rest of the grid is fully unstructured and consists of tetrahedral elements of characteristic length that range from 3.6×10^{-4} to 2.3 m.

Large eddy simulation

LES relies on a spatial decomposition of the flow scales by means of a filtering operation on the total quantities; the decomposition is meant to allow the explicit resolution of the large eddies while modeling those that are smaller than the grid spacing. Each velocity component u_i (i=1–3) and pressure p are decomposed into grid-resolved and unresolved quantities such that $u_i = \tilde{u}_i + u'$ and $p = \tilde{p} + p'$. With the tilde and prime symbols identifying the resolved and unresolved quantities, respectively, the filtered Navier–Stokes equations of incompressible flows are written as:

$$\frac{\partial \tilde{u}_i}{\partial t} + \frac{\partial \tilde{u}_i \tilde{u}_j}{\partial x_j} = -\frac{1}{\bar{\rho}}\frac{\partial \bar{\rho}}{\partial x_i} + \nu \frac{\partial^2 \tilde{u}_i}{\partial x_j^2} + \frac{\partial \tau_{ij}}{\partial x_j}, \quad (1)$$

where ρ is the water density, ν is the kinematic viscosity and $\tau_{ij} = \widetilde{u_i u_j} - \tilde{u}_i \tilde{u}_j \approx -2\nu_e S_{ij} + \tau_{kk}\delta_{ij}/3$ [i,j,k=(1–3)=x,y,z)] is the stress tensor evaluated at the level of unresolved scales. In this expression, S_{ij} and δ_{ij} are the rate of strain and the Kronecker delta function, respectively. The definition of the eddy viscosity, ν_e, dictates the type of LES model. The Vreman subgrid scale eddy viscosity model (Vreman, 2004) was used in this study, with a Smagorinsky model constant of 0.1. The incompressibility is

Journal of Experimental Biology (2020) 223, jeb226654. doi:10.1242/jeb.226654

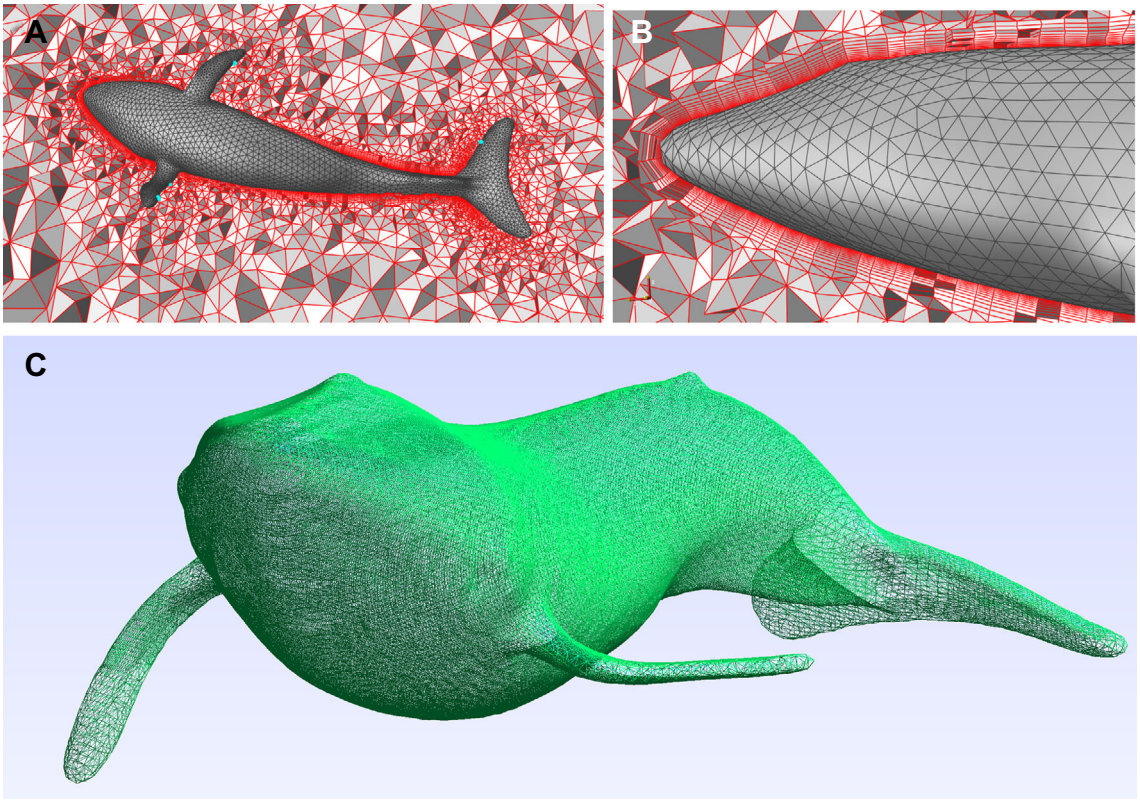

Fig. 3. Visualizations of the computational grids around the whale's body. For clarity of visualization, the plotted meshes are coarser than the ones used in the simulations. (A) Ventral view of the whale surface grid with a selection of the volume grid around it. (B) Close-up view of the boundary layer mesh around the whale's head. The grid is fully unstructured and consists of tetrahedra in the majority of the volume and prisms in the boundary layer regions (right). (C) Stereolithography of the scanned whale replica.

imposed via the solenoidal equation $\partial_i u_i=0$ (summation is understood on the repeated indices).

The grid requirements to resolve all the important scales in the viscous sub-layer of a wall-bounded flow increase with increasing Reynolds numbers. Wall-resolved LES (WRLES) is hence still limited to moderate Reynolds numbers because of the high computational cost required to capture the eddies in the inner boundary layer. A Reynolds number $Re_c \approx 22.7\times10^6$ makes WRLES infeasible; WRLES is much too costly because of prohibitive grid resolution requirements in the proximity of the solid walls (Bose and Park, 2018). Instead, a computationally affordable alternative is provided by what is referred to as wall-modeled LES (WMLES) (Larsson et al., 2016; Piomelli, 2008; Piomelli and Balaras, 2002; Shur et al., 2008), which is what was utilized in this study. WMLES provides more affordable LES by modeling the near-wall layer. The grid resolution requirements in the proximity of the wall are relaxed according to the following estimates (Bose and Park, 2018; Choi and Moin, 2012) of grid point count within a differential volume $dV=\delta dx_1 dx_2$ (where δ is the local boundary layer thickness and dx_1 and dx_2 are, respectively, the volume size in the stream-wise and span-wise direction). By indicating the wall shear stress with τ_w and using the superscript + to indicate wall units, the number of grid points necessary for WRLES (WR) is given by:

$$dN_{WR} = \frac{n_{x_3}}{\Delta x_{1_w}^+ \Delta x_{2_w}^+} \frac{\tau_w dx_1 dx_2}{\rho \nu^2}, \quad (2)$$

where $\Delta x_{1_w}^+$ and $\Delta x_{2_w}^+$ are the grid spacing in the stream-wise and span-wise directions within the boundary layer. The quantity n_{x_k} denotes the number of grid points within a length δ in the x_k direction. By contrast, the number of grid points necessary for a WMLES (WM) to resolve the same length delta in the wall normal direction is:

$$dN_{WM} = \frac{n_{x_1} n_{x_2} n_{x_3} dx_1 dx_2}{\delta^2}. \quad (3)$$

The integration of dN_{WR} and dN_{WM} in the stream- and span-wise directions yields the following scaling with respect to the Reynolds number based on the whale length c:

$$[N_{WR} \sim Re_c^{13/7} \quad \text{versus} \quad N_{WM} \sim Re_c], \quad (4)$$

with a clear indication of the enormous computational savings if WMLES is used. This is the reason why only 8 elements in the wall normal direction were used in the boundary layer grid described above.

Boundary conditions and wall model

LES requires the imposition of the wall shear stress at solid boundaries to ensure momentum conservation in the first cell from the wall (Bose and Park, 2018). In the case of WMLES, the inner layer is unresolved, and the wall shear must be derived from the velocity calculated at some non-dimensional distance y^+ from the wall. In the simulations described in this study, the finite element extension by Owen et al. (2019) of the wall law of Reichardt (1951) was used:

$$u^+ = \frac{1}{\kappa}\ln(1+\kappa y^+) + 7.8\left(1 - e^{-y^+/11} - \frac{y^+}{11}e^{-0.33y^+}\right), \quad (5)$$

Journal of Experimental Biology (2020) 223, jeb226654. doi:10.1242/jeb.226654

where κ is the von Kármán constant, $y^+=yu_\tau/\nu$ for $u_\tau=(\tau_w/\rho)^{1/2}$ and $u^+=u/u_\tau$ (throughout the paper, y indicates the coordinate that is locally orthogonal to the whale surface). To treat the pathological log-layer mismatch issue that characterizes all wall models, the local time filtering of Yang et al. (2017) was applied in our simulations.

Estimation of the boundary layer thickness

Boundary layer profiles and thickness, including displacement and momentum thickness, were determined in various regions (Fig. 4) of the whale. By definition, the boundary thickness (δ) is the distance from the surface beyond which the flow becomes irrotational; in good approximation, it was measured as the distance within which the flow velocity reaches 99% of the free stream velocity, U_0. The displacement and momentum thickness are a more precise way to estimate the boundary layer extension; they were also calculated by means of their analytical definitions:

$$\delta^* = \int_0^\infty \left(1 - \frac{u}{U_0}\right) \mathrm{d}y \tag{6}$$

and

$$\theta = \int_0^\infty \frac{u}{U_0}\left(1 - \frac{u}{U_0}\right) \mathrm{d}y. \tag{7}$$

Fig. S3 shows a sample of boundary layer profiles and their various thickness parameters.

Pressure, friction and drag coefficients

We report pressure, friction and drag coefficients in Fig. 5B and Table S1. Our pressure and friction coefficients, C_p and C_f, are local coefficients, representing the dynamic pressure and wall shear stress at a given position on the body surface and scaled by the stagnation pressure, $(1/2)\rho U_0^2$, as is customary, i.e.

$$C_p = \frac{p - p_0}{(1/2)\rho U_0^2} \tag{8a}$$

and

$$C_f = \frac{\tau_w}{(1/2)\rho U_0^2}. \tag{8b}$$

In Eqn 8ab, p is the local pressure on the surface, p_0 is the value of the pressure in the free stream far from the organism and τ_w is the local wall shear stress. These local coefficients are used to find the pressure and friction forces on each facet of the surface of the whale or remora from the computational grid and the components of those forces in the direction of swimming are added up to get total drag, D, in the swimming direction. This total drag can then be used to determine the total drag coefficient, C_d, that encompasses the effects of both pressure and friction drag:

$$C_d = \frac{D}{(1/2)\rho U_0^2 A}, \tag{9}$$

where A is either projected frontal area or total wetted area. In Table S1, we report values of C_d using both areas for comparison with values in the literature. The only exception is that in the case of the flippers, in addition to total wetted area, the planform area was used to calculate C_d, as is customary for wing-like objects.

The small value of the whale's body drag coefficient (Table S1) supports the above observations that the flow around the whale body is almost fully attached with very few, localized regions of separation and reattachment of the boundary layer. The sudden variations in friction shown in Fig. 5B indicate some of these points of separation and reattachment. However, our model did not include small-scale roughness; a smooth surface was assumed. Given the instability of the boundary layer in the simulations, roughness could easily trigger a fully turbulent boundary layer in some or most of the regions where the structure of the vorticity and velocity profiles suggest that the boundary layer remained transitional in our simulation (Figs 3 and 4; Figs S2–S4). This could lead to higher drag predicted for the whale and an attached remora, but as it is likely to increase the drag at all locations, the effect is not expected to change the conclusions about which regions have the least drag and whether those regions are preferred by remora.

Computational resources

The computational mesh consists of 41,926,192 finite elements and 9,001,098 grid points. To reach a steady state, the simulations were executed for 48 h using 720 cores (approximately 35 thousand core hours) on MareNostrum IV at the Barcelona Supercomputing Center. The mesh with the inclusion of the remoras has approximately the same number of grid elements and grid points. The same number of computing cores was utilized for both sets of simulations (with and without remoras). The empirical approach allowed us to calculate the drag reduction at all 32 locations on the whale after just one CFD simulation to get the boundary layer flow.

Drag reduction calculations by empirical analysis

Whether a body experiences lower drag attached to a surface (D_{BL}) than in the freestream (D_{FS}) depends on body size and shape and the surface boundary layer in an unexpectedly complicated way. In general, the drag on an object attached to a surface and residing entirely in the boundary layer decreases as that object decreases in height – even if its frontal area remains constant. It experiences lower flow velocities deeper in the boundary layer and, generally, lower form drag. However, our CFD simulation of flow over a whale predicted that boundary layer thickness was not always greater than possible heights of the remora. Thickness ranged from 0.4 to 3.5 cm in separation of flow (S) regions, 0.7 to 24.4 cm in wake (W) regions, and 0.1 to 3.6 cm in regions where no remoras were observed (NR), while the typical remora sizes we considered ranged up to 5.3 cm (h_{max}). Still, one might expect that residing even partly in a boundary layer would lead to a benefit over swimming or coasting in the freestream as the full velocity profile faced seems always to carry with it at least some momentum deficit compared with the freestream. But this turns out not to be the case. The reason is 'interference drag'. Interference drag originates from the flow disruption caused by two bodies being close or connected in a flow (Hoerner, 1965). It is well known in marine hydrodynamics that the drag on a submarine with a conning tower is more than the sum of the drag on the hull and conning tower studied separately (Joubert, 2004); and the effect can be quite significant. A fared dimple, like a cockpit canopy, on a flat surface can have a drag more than 2 times the drag on the canopy shape in the freestream (Hoerner, 1965). Calculating drag on such bodies using drag coefficients is not straightforward. Standard constant coefficients of drag for an object in a freestream, or uniform flow, C_{DFS}, cannot be used to account for interference drag. The actual drag coefficient for a body attached to a

Journal of Experimental Biology (2020) 223, jeb226654. doi:10.1242/jeb.226654

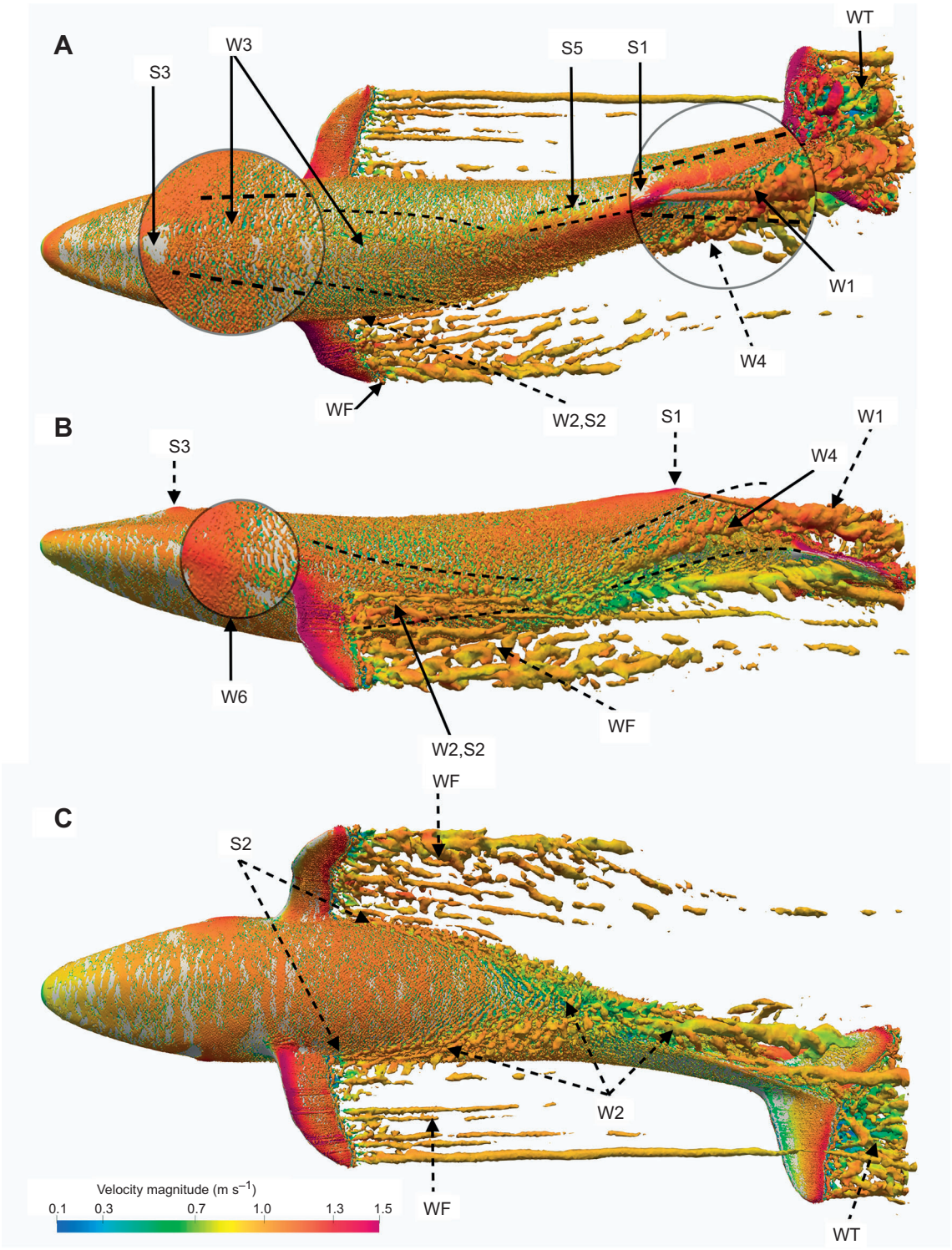

Fig. 4. The vorticity field represented by means of the *Q*-criterion (Hunt et al., 1988). Dorsal (A), lateral (B) and ventral (C) views. Vorticity is colored by velocity magnitude at the outer edge of the boundary layer, revealing structure in the flow, including small-scale instabilities over much of the surface as in transitional flow, and large-scale vortical flows typical of wakes and separation zones. Velocity can be used in this figure as a first-order qualitative proxy for wall shear stress (e.g. note the low velocities in the W2 wake region, which offers some of the best drag reduction for remora according to this work). S numbers are separation points; W numbers are wake regions (delineated by dashed lines); WT, tail wake; WF, flipper wake.

surface, C_{DBL}, changes with its height-to-boundary layer thickness ratio and body shape. Instead, a so-called 'independent drag coefficient', c_D, is used, which is generally constant for body heights up to 2 times boundary layer thickness (Hoerner, 1965). The area-averaged dynamic pressure on the frontal area of the body – the 'effective dynamic pressure' – is then used instead of the standard dynamic pressure, $(1/2)\rho U_0^2$ (Hoerner, 1965). This results in a varying drag coefficient, C_{DBL}, that can be calculated from the

Journal of Experimental Biology (2020) 223, jeb226654. doi:10.1242/jeb.226654

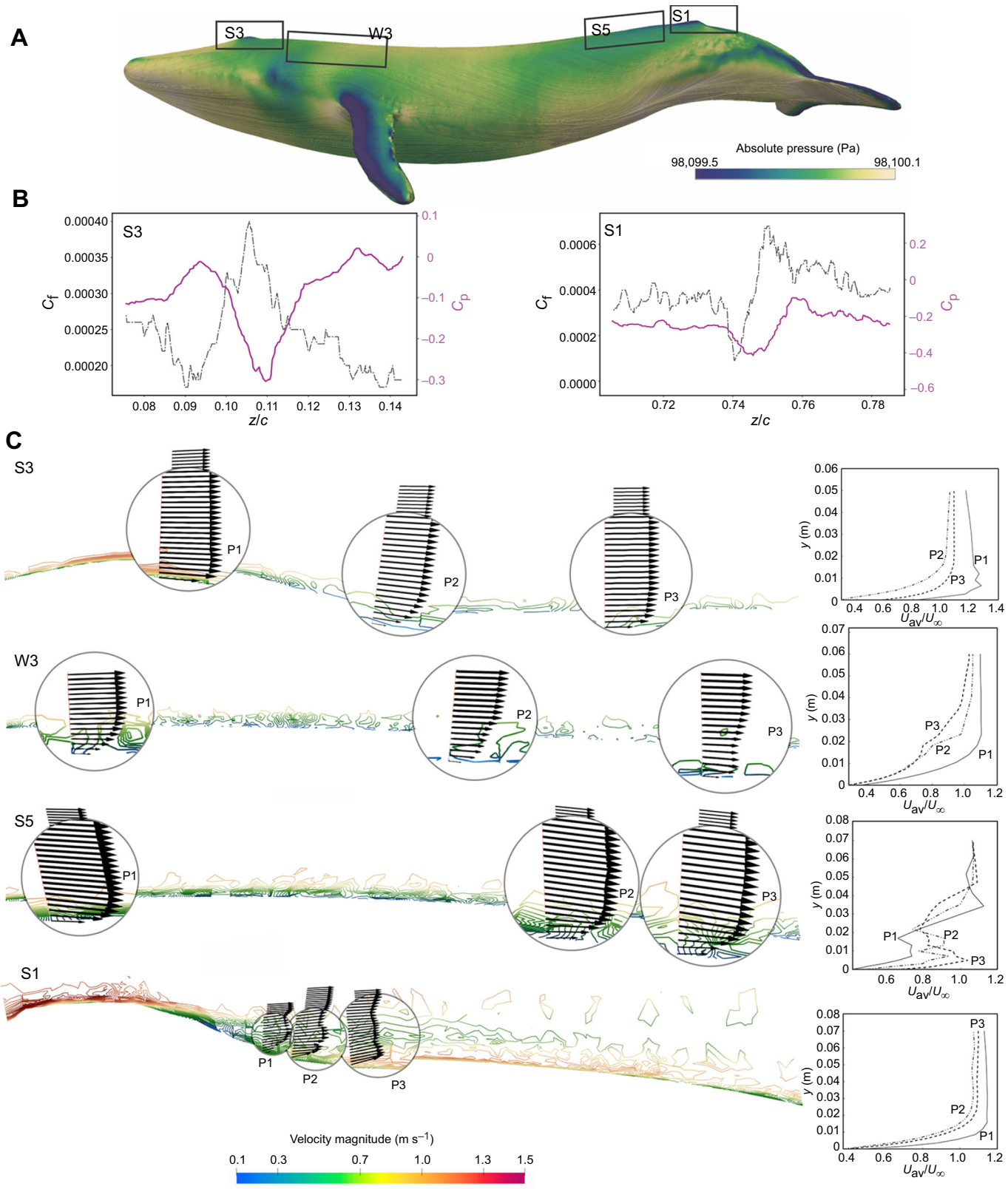

Fig. 5. Pressure, friction and streamlines. (A) Streamlines over the body of the whale colored by pressure. (B) Coefficient of friction (C_f, black dot–dash line) and coefficient of pressure (C_p, purple solid line) at the blowhole (S3) and dorsal fin (S1); z is the distance from the leading edge, c is body length. (C) Close-up of streamlines at the blowhole (S3), dorsal fin (S1), flank behind the blowhole (W3) and ridge anterior to the dorsal fin (S5), colored by vorticity magnitude. The four panels on the right show the time-averaged instantaneous streamwise velocity (U) profiles measured at P1, P2 and P3 along the whale surface at regions S3, S1, W3 and S5. A sample of these profiles is shown in wall units in Fig. S1.

Journal of Experimental Biology (2020) 223, jeb226654. doi:10.1242/jeb.226654

independent drag coefficient using:

$$C_{DBL} = \frac{c_D \iint (1/2)\rho[u(y)]^2 dA}{(1/2)\rho U_0^2 A_f}, \quad (10)$$

where ρ is the fluid density (which cancels), U_0 is the freestream flow speed, A_f is the frontal area of the body, dA is an infinitesimal area element on the frontal area and $u(y)$ is the oncoming velocity profile experienced by the body. Drag reduction is present if the fraction of the difference in drag between the attached state and the freestream, i.e.

$$\frac{D_{BL} - D_{FS}}{D_{FS}} = \frac{C_{DBL}}{C_{DFS}} - 1, \quad (11)$$

is negative.

Attached remoras happen to be shaped like an optimal streamlined surface dimple shown in Hoerner (1965), and empirical data from the field of aerodynamics shows that the independent drag coefficient, c_D, of such objects is 0.04 (Hoerner, 1965). The remora body height-to-length ratio of about 10–12 is ideal in aerodynamic dimples, and the small angle of the leading end of the body is a shape known to decrease interference drag. Dimples with a steeper increase in leading-end height, as in a submarine conning tower, have much higher interference drag. The half-ellipse cross-section of the remora places most of its frontal area lowest in the boundary layer, lowering the effective dynamic pressure. The c_D value of 0.04 and the boundary layer profiles from our CFD were used in Eqn 10 to calculate C_{DBL} for remora. For use in Eqn 11, a very conservative estimate of the standard constant drag coefficient, C_{DFS}, of 0.03 was used. This is actually the value for a rigid, remora-shaped body of revolution in the freestream – a shape like two remora connected at their dorsal surfaces. C_{DBL} and C_{DFS} were then used in Eqn 11 to compare the drag of the attached and freestream states and determine whether there is drag reduction in the attached state. The actual drag reductions may be of greater magnitude than reported here as work on swimming fish suggests that friction drag, and thus potentially the freestream drag coefficient (C_{DFS}), is higher on swimming fish than a fish coasting or 'stretched-straight' in a flow (Anderson, 2005; Anderson et al., 2001; Lighthill, 1971). This may even be true in the case of remora heights exceeding 2 times the boundary layer thickness, in which the contribution of decreased momentum in the boundary layer to drag in the attached state decreases in comparison to that of the flow over the section of the body outside of the boundary layer. One would expect the situation to converge toward no drag reduction, but low interference drag due to the favorable remora shape and higher drag in undulatory swimming versus coasting may lead to higher drag reduction than we calculate, and even where Eqn 11 yields no drag reduction.

Experimental remora–host interaction fluid dynamics

Fluid dynamic analysis of one preserved *Remora australis* remora (32.6 cm total length) in a flume with a working section 170×45×45 cm (Engineering Laboratory Design, Lake City, MN, USA) was performed at the Woods Hole Oceanographic Institution Shore Laboratory (WHOI, Falmouth, MA, USA). Flow was maintained at 20 cm s^{-1}, slower than the 1.5 m s^{-1} used in the simulation, but potentially similar to a small remora swimming close to the whale surface in a wake region on the whale body. A vertical light sheet was produced using a pulsed IR laser (Firefly, 300 W, 808 nm; Oxford Lasers, Shirley, MA, USA). The flow was seeded with neutrally buoyant 50 µm plastic particles and imaged using a digital video camera (SA-3, 1024×1024 pixels, 60 frames s^{-1}; Photron, San Diego, CA, USA) with a macro photographic lens (Micro-Nikkor, 105 mm; Nikon, Melville, NY, USA) to obtain high-resolution images of a field of view of 12.5×12.5 cm. The TTL synchronized camera recorded at 60 Hz and, therefore, image pairs were acquired at 30 Hz. The camera and laser were both mounted on a robotic positioning system built at WHOI for use with the flume. This was used to move the laser and camera field of view along the remora body at 7.5 cm intervals to reconstruct flow over the entire body in high resolution. Velocity fields were calculated from the particle images using an off-the-shelf PIV analysis software package (DaVis; LaVision Inc., Ypsilanti, MI, USA). Velocity vectors were calculated from image sub-windows 32×32 pixels in size with 50% overlap, resulting in a grid of 64×64 vectors for each image pair. The velocity fields from 150 image pairs at each field of view along the remora were used to calculate an average velocity field.

RESULTS

Eleven tag deployments on three individual blue whales resulted in 211.5 min of video footage containing a total of 27 remoras observed at 61 locations on the whales. Remoras were identified from surface photographs and video sequences as *Remora australis* (Figs 1 and 2) and were estimated to be 20–40 cm BL based on proximity to the camera tag and whale morphology. Remoras were most often observed directly behind the blowhole, next to and behind the dorsal fin, and on the flank region above and behind the pectoral fin (Figs 1 and 2). In two of these regions, behind the blowhole and around the dorsal fin, remoras were observed to cluster. Notably, remoras maintained attachment to these locations during whale surfacing, which resulted in the remoras being completely out of the water for a short time. Remoras also often attached near the camera tag on the dorsal surface of the whale body (Movie 1). Two tag deployments that ended in the tag sliding around the lateral and ventral aspects of the whales did not show any remoras on the ventral surface, nor did the video sequences captured underwater by divers. Rayleigh's test for non-uniform distribution showed that the remora positions were significantly different from random (P=0.01). This indicates attachment location preference and clustering in specific locations on the whale body.

Remoras need not keep a stationary position to maintain attachment to the whale. Instead, remoras were commonly observed to lift off the whale to feed and then return to their previous position (Movie 2), or other positions on the whale. Positional changes were often accomplished by a skimming behavior (Fig. 2D; Movie 3), in which a remora maintained a distance of a couple centimeters or less above the body of the whale, swimming in a slow and controlled fashion. Skimming behavior of remoras was observed while the whale velocity was between 1.5 and 3 m s^{-1}, and our observations suggest that remoras were not experiencing freestream conditions, which were approximately 1–3 BL s^{-1} for the largest known remoras recorded and as high as 15–20 BL s^{-1} in some of the smaller remora we consider here. Remoras also changed position using a sliding behavior (Movie 4), in which their disc maintained contact with the whale while they swam. Tail beat frequency of remoras exhibiting skimming and surfing behaviors was 0.5–2 Hz, whereas remoras swimming in the freestream above the whale used tail beat frequencies of 5–8 Hz.

CFD model of whale boundary layer

A fine-scale numerical simulation of the flow around an 18 m blue whale was used to provide flow field information for empirical calculations of drag on attached remora. We used these drag

calculations to explore the possibility that remoras select their position on the whale surface based on local hydrodynamic conditions. The simulation showed that the boundary layer remains mostly attached along the body surface except for specific regions where separation of flow (S regions) and wakes (W regions), both due to surface features, was observed. In Fig. 4, fluid structure revealed by vorticity near the whale surface shows that separation is triggered by protuberances on the whale surface, specifically the blowhole, the dorsal ridges and dorsal fin. In addition, the flippers and tail flukes exhibit significant flow separation. Turbulent wakes often develop downstream from the separation regions as flow fails to reattach. Furthermore, it was observed that the boundary layer is transitional, not fully turbulent, along most of the whale body, based on the large scale and intermittent structure in the near-wall vorticity (Fig. 4) and boundary layer profile shape (Fig. 4; Figs S2–S4). Tangential velocity profiles often exhibited inflections, a common sign of instability, and almost without exception their shapes fell between that of laminar and fully turbulent profiles, also a sign of transition (Wang et al., 1996; Schlichting and Gersten, 2000). This indicates that although some body features may cause separation-triggered turbulence, the modeled surface features are not sufficient to sustain a fully turbulent boundary layer. Still, as mentioned above, we did not include small-scale surface roughness that could result in a fully turbulent boundary layer, and this could impact our calculations of drag on remora. Nevertheless, in regions of separation and wakes due to large surface structures on the whale, where more remora were observed, we expect boundary layer profiles to exhibit more instances of decreased momentum than in less obstructed regions where few to no remora are observed. The latter regions would be more likely to exhibit the typical high shear boundary layer profiles of fully turbulent boundary flow. Therefore, though our absolute drag values may be underestimates if the boundary layer flow is indeed fully turbulent, remora seeking lower drag would still be expected to attach in regions identified as having relatively lower drag by our analyses.

Drag reduction in attached remora

We determined the fraction of drag difference between the attached state and coasting in the freestream (Eqn 11) in remora at 32 locations within 10 regions on the whale surface (Fig. S4) where three types of flow were observed (Fig. 4): four regions near flow separations (S), three in the wakes of surface structures (W) and three regions of well-attached flow where few to no remora were observed to attach (NR). For ease of presentation, we ran calculations for remoras of four body heights: 0.2, 0.5, 0.9 and 1.0 times h_{max}, 5.3 cm, a height representing the 90th percentile for the species of remora we observed. We found that in the attached state, remora 0.2 times h_{max} in height experience 40–50% drag reduction in S regions, 59–84% in W regions and 6–25% in NR regions compared with coasting in the freestream. Remora 0.5 times h_{max} in height experience 0–38% drag reduction in S regions, 25–78% in W regions and 0–2% in NR regions. The tallest remoras were found to experience significant drag reduction in one of the S regions (S1, 3–8%), two of the W regions (W2, W3, 13–73%) and none of the NR regions. As mentioned above, any increase in the freestream drag coefficient, C_{DFS}, over the conservative estimate of 0.03 used here yields greater drag reduction. A coefficient just 33% higher (0.04) results in drag reduction for remora of almost every size at nearly every location except at zone NR3 (Fig. S5). In general, drag reduction is highest in the W regions and lowest in the NR regions. Drag did not exceed 0.30 N for any attached remora analyzed at any location. This agrees with a straightforward estimate of 'stretched–straight', or rigid-body, drag on a remora h_{max} in height in the freestream using C_{DFS}=0.03.

We did the same analysis for a remora skimming anteriorly on the whale at a speed of 0.5 BL s^{-1} and a height of 1–2 cm above the surface. The behavior increases drag, as expected, but fish 0.2 times h_{max} in height experience drag reduction at 9 locations skimming 1 cm off the surface (Fig. S6) and 6 locations at 2 cm off the surface (Fig. S7). In every case, only S and W regions offered drag reduction during skimming in remora; NR regions did not. Some S region locations offered drag reduction in skimming for fish heights up to 0.49–0.57 times h_{max}, and in W regions, 1.0 times h_{max} and larger. Skimming fish are swimming and, therefore, drag may be higher than we estimate as a result of body undulation, but remora swimming in the freestream would also have to undulate, and more vigorously, as was evident by the lower tail beat frequency of skimming and sliding remoras as compared with those swimming in the freestream. Also, a less pronounced or lack of drag reduction in skimming does not outweigh the benefits of attachment, but it might affect where remoras of particular sizes choose to attach.

The impact of interference drag on attached remora can also be taken into account through a well-resolved CFD analysis. We used remora body geometry from a CT scan and performed an additional CFD simulation with a remora attached at 3 of the 32 locations (Fig. 6). We also used CFD to calculate the rigid body drag of the remora in the freestream. We then compared our empirical result at the same locations with this full CFD approach. Our CFD predicted a drag reduction of 17% at S3 in a remora of about 0.2 times h_{max} in height (Fig. S4). Our empirical method predicted 42%. It could be argued that this suggests that the empirical method overpredicts drag reduction, but the accuracy of the CFD approach is limited by the grid resolution of the simulated remora due to the large size of the whale and therefore lower resolution of the computational grid at the scale of the remora. We hold that the fact that the two methods are reasonably close and both predict drag reduction is compelling complementary support of the results of our empirical approach, and thus our hypothesis. Our data show that remora congregate in S and W regions, where there is more drag reduction available, and not in NR regions, where there is far less drag reduction.

Remora–fluid–surface interactions

Particle image velocimetry (PIV) of a remora (*R. australis*) within a few centimeters of a surface revealed another physical phenomenon that might be important for helping remoras return to contact with their hosts while changing position. As a remora approaches a host surface (Fig. 7A), the narrowing at the entrance to the space between the remora and the host surface results in an acceleration of fluid so that flow between the remora and the surface is faster than freestream (Fig. 7B). Therefore, the fluid pressure between the remora and the surface is possibly lower than the surrounding fluid – a phenomenon known as the Venturi effect. The resulting suction effect may help the remora stay close to the host while it is temporarily detached.

DISCUSSION

Some remoras, such as *R. australis*, are known to be specific to cetaceans but other host-generalist species, such as *Echeneis naucrates*, also frequently attach to whales and dolphins, among others (Fertl and Landry, 1999; O'Toole, 2002; Silva-Jr and Sazima, 2003). Remora attachment locations on host organisms are known primarily through fishery landing reports, photographs and anecdotal information. By using opportunistically recorded

Journal of Experimental Biology (2020) 223, jeb226654. doi:10.1242/jeb.226654

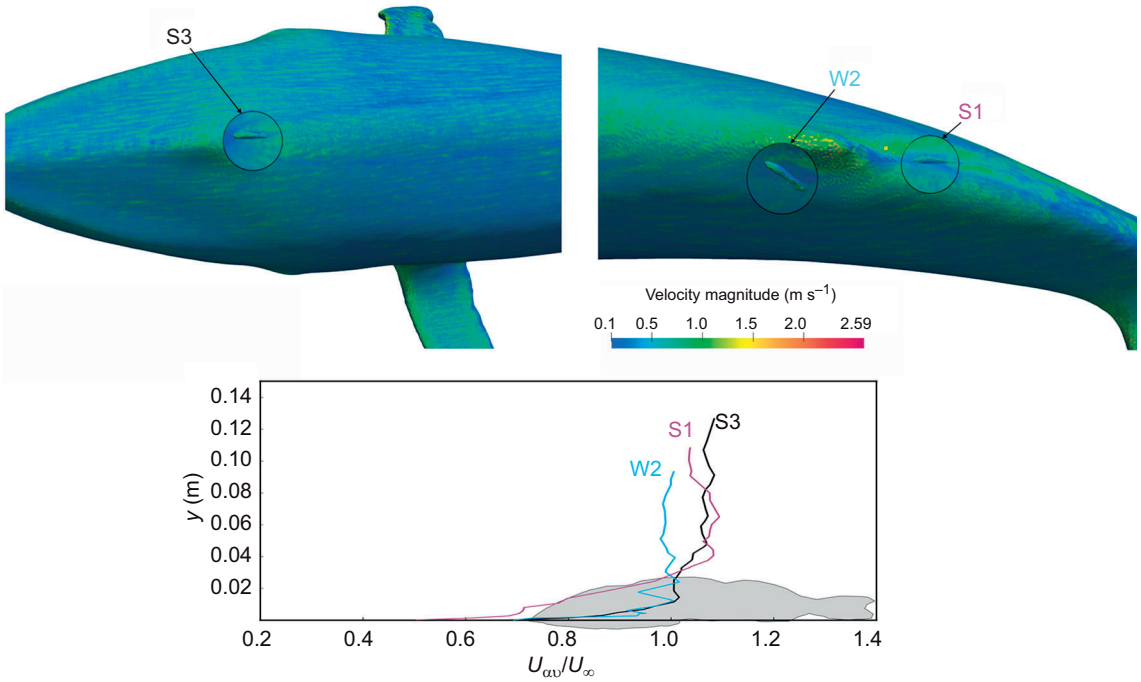

Fig. 6. Dorsal view with magnified insets of remora placement used in computational fluid dynamic analyses and average streamwise velocity profiles for each region. Remora were placed at the blowhole (S3, black), dorsal fin (S1, purple) and flank beside the dorsal fin (W2, blue). The gray silhouette of *Remora australis* (total length 30 cm, average size seen on whales) is included for reference.

camera-tag video data, the work presented here is the first continuous recording of remora behavior on a host organism, allowing for behavioral observations of individual remoras for extended periods of time. Our work provides strong evidence that remora preferentially select regions offering lower drag and, in particular, regions near separation of flow caused by surface features and in the wakes that develop downstream of those regions. While remoras were observed in other locations that offered little to no drag benefit, those individuals were fewer in number, typically smaller in size, and were in some cases observed later moving to a region offering lower drag. Interestingly, remoras were not observed on the ventral surface of the whales, which might be a location with the advantage of being less susceptible to sea bird predation (Sazima, 2018). Moreover, during surfacing, remoras maintained their attachment on the dorsal aspect of the whales and did not detach or move to maintain a submerged, and potentially more protected, position.

We observed behaviors in remora that we refer to as ‘skimming’ and ‘sliding’. Skimming, or swimming and gliding very close to the whale surface, allows the remora to change to a more lateral or

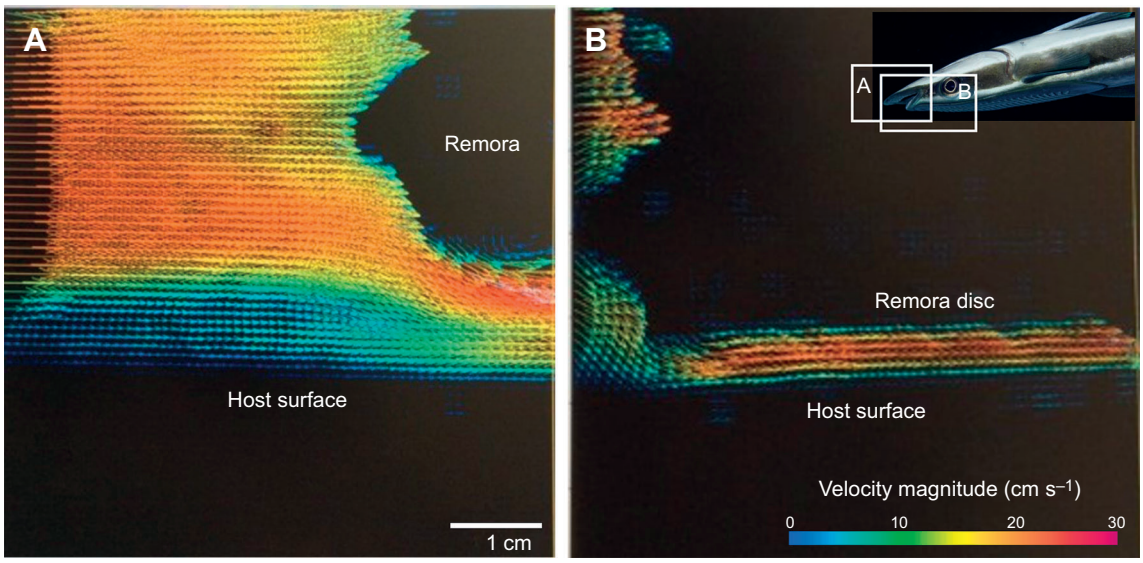

Fig. 7. Particle image velocimetry images of the lateral view of a remora approaching a flat ‘host’ surface in a flow tank. Flow is moving from left to right. (A) Lateral view of flow under the anterior aspect of the remora rostrum as it approached the host surface. (B) Lateral view of accelerated flow between the remora and host at 1 cm distance.

caudal position with little to no swimming effort, and to swim upstream with reduced effort if the remora is small enough and close enough to the whale to experience drag reduction. In general, however, there is very little drag reduction while skimming and the remora most likely take advantage of their streamlined shape to skim with ease. When skimming within a couple of centimeters of the surface of the whale, the Venturi effect may, in part, help the remora maintain proximity to the whale while traveling parallel to the whale body, which facilitates reattachment and, in some regions, helps to keep the remora in the reduced flow of the boundary layer. Of course, the curved ventral surface of the remora is expected to lead to a low-pressure zone, and thus lift, that would tend to pull the remora away from the whale. So, a low-pressure region between the whale and a skimming remora may simply counteract that lift force.

The sliding behavior of remoras involves two mechanisms that contribute to remora adhesion: suction and friction. Remora adhesion is accomplished when the dorsally located adhesive disc is pressed against a host surface and serially arranged bony lamellae rotate. The outer edge of the disc is composed of a fleshy lip that seals the disc to the host surface and a suction force is generated by the negative pressure space created by lamellar rotation (Beckert et al., 2015; Fulcher and Motta, 2006). Aside from friction due to the contact of the two surfaces, additional resistance to shear is generated when small pointed spinules on the lamellae engage with local surface roughness of the host. Friction force contributed by the spinules has been estimated by measuring the shear force needed to slide a remora along rough and smooth surfaces (e.g. Plexiglas; Beckert et al., 2015; Fulcher and Motta, 2006; Gamel et al., 2019). One study measured the maximum shear forces at adhesive failure to be 17 and 11 N on rough and smooth surfaces, respectively, showing that the spinules contribute significantly to attachment via friction (Beckert et al., 2016b; Fulcher and Motta, 2006). We calculated shear forces on remora attached to a whale swimming 1.5 m s^{-1} to be no more than about 0.3 N, well below either of these values. Even on a whale swimming at 3.9 m s^{-1}, we would expect drag of no more than 2–4 N. This suggests that while we found remoras to locate in low drag regions on a whale, they are probably capable of remaining attached almost anywhere on even a fast-swimming whale. Their selection of low drag regions is therefore not a necessity as much as an advantage that would decrease energy needed to remain attached and, to some extent, move about the whale surface. This makes sense of our observation that remora occasionally attached to the whale's tail where they would certainly experience high drag at times.

As remoras stay in contact with the whale surface during sliding, it seems that some suction is maintained while the lamellae may not be rotated enough to create significant spinule contact with the surface. This suggests that remoras can actively modulate the position of their lamellae and still maintain attachment to a host surface while under shear conditions. This ability could be important for clearing fluid out of the disc while attached, especially if seep due to the pressure difference between the inside and outside of the disc could causes suction loss (Beckert et al., 2016b; Flammang and Kenaley, 2017).

Our work represents the highest resolution whole-body fluid dynamic analysis to date of the world's largest vertebrate. Knowledge of blue whale hydrodynamics has broad-reaching implications for understanding their ecology and physiology, especially with consideration to analyzing the metabolism of a migratory animal. For example, this will inform the study of energetic expenditure in swimming, prey reactions to turbulent flow around a predator, and maneuverability, which depends on forces generated by control surfaces. In addition, understanding the flow environment around a swimming blue whale could help inform the placement of tags and new technology so they are more likely to remain attached to the animal (Gamel et al., 2019). Current tag technology, like that used to collect the video data used here, are restricted to suction cup attachments, which can fail within hours and rarely remain attached for more than 48 h. It is our hope that better understanding of both the flow environments around an organism and the mechanisms by which specifically adapted organisms like remoras successfully attach to hosts will help to inspire new technologies and designs for behavioral and ecological monitoring.

Acknowledgements
We are extremely thankful for the support and contributions of the following people: S. Soletto and Z. Zahid assisted in spotting remoras in videos and preliminary theoretical drag calculations; L. Natanson, NOAA Fisheries, provided frozen remoras of unusual size; L. Winn worked on an initial scan of the blue whale model; I. Malcom, University of Texas Austin, gave insightful comments.

Competing interests
The authors declare no competing or financial interests.

Author contributions
Conceptualization: B.E.F.; Methodology: B.E.F., S.M., O.L., E.J.A., D.E.C., J.C., A.S.F., J.A.G.; Software: G.H., M.V., D.E.C. Formal analysis: B.E.F., S.M., O.L., E.J.A., A.M., D.E.C. Investigation: B.E.F., S.M., O.L., E.J.A., M.B., J.H.N.; Resources: O.L., E.J.A., G.H., M.V., J.C., A.S.F., J.A.G.; Data curation: D.E.C., H.E.A.; Writing - original draft: B.E.F., S.M.; Writing - review & editing: B.E.F., S.M., O.L., E.J.A., D.E.C., M.B., J.H.N., H.E.A., J.C., A.S.F., J.A.G.; Visualization: B.E.F., O.L., E.J.A., A.M.; Supervision: B.E.F.; Project administration: B.E.F.; Funding acquisition: B.E.F., S.M., E.J.A., J.A.G.

Funding
Financial support was provided by Stanford University and a Terman Fellowship to J.A.G., the Ministerio de Economía y Competitividad, Secretaría de Estado de Investigación, Desarrollo e Innovación, Spain (ref. TRA2017-88508-R) to O.L., a grant from the Grove City College Swezey Fund to E.J.A., and New Jersey Institute of Technology to B.E.F. Additional support for tagging and filming operations came from the National Oceanic and Atmospheric Administration (NOAA) and the BBC. The Barcelona Supercomputing Center awarded access to the MareNostrum IV machine (Barcelona, Spain).

Supplementary information
Supplementary information available online at
https://jeb.biologists.org/lookup/doi/10.1242/jeb.226654.supplemental

References
Anderson, E. J. (2005). Advances in the visualization and analysis of boundary layer flow in swimming fish. *PhD thesis, Woods Hole Oceanographic Institution*. doi:10.1575/1912/1581

Anderson, E. J., McGillis, W. R. and Grosenbaugh, M. A. (2001). The boundary layer of swimming fish. *J. Exp. Biol.* **204**, 81-102.

Andrade, Á. B. (2007). Echeneis naucrates (Linnaeus) (Perciformes, Echeneidae), unusual interaction with a diver. *Pan Am. J. Aquat. Sci.* **2**, 42-50.

Beckert, M., Flammang, B. E. and Nadler, J. H. (2015). Remora fish suction pad attachment is enhanced by spinule friction. *J. Exp. Biol.* **218**, 3551-3558. doi:10.1242/jeb.123893

Beckert, M., Flammang, B. E., Anderson, E. J. and Nadler, J. H. (2016a). Theoretical and computational fluid dynamics of an attached remora (*Echeneis naucrates*). *Zoology* **119**, 430-438. doi:10.1016/j.zool.2016.06.004

Beckert, M., Flammang, B. E. and Nadler, J. H. (2016b). A model of interfacial permeability for soft seals in marine-organism, suction-based adhesion. *MRS Adv.* **1**, 2531-2543. doi:10.1557/adv.2016.445

Bose, S. T. and Park, G. I. (2018). Wall-modeled large-eddy simulation for complex turbulent flows. *Annu. Rev. Fluid Mech.* **50**, 535-561. doi:10.1146/annurev-fluid-122316-045241

Brazier, K. T. S. (1994). Confidence intervals from the Rayleigh test. *Mon. Not. R. Astron. Soc.* **268**, 709-712. doi:10.1093/mnras/268.3.709

Brunnschweiler, J. M. and Sazima, I. (2006). A new and unexpected host for the sharksucker (*Echeneis naucrates*) with a brief review of the echeneid–host interactions. *Marine Biodiversity Records* **1**, E41. doi:10.1017/S1755267206004349

Cade, D. E., Friedlaender, A. S., Calambokidis, J. and Goldbogen, J. A. (2016). Kinematic diversity in rorqual whale feeding mechanisms. *Curr. Biol.* **26**, 2617-2624. doi:10.1016/j.cub.2016.07.037

Cade, D. E., Barr, K. R., Calambokidis, J., Friedlaender, A. S. and Goldbogen, J. A. (2018). Determining forward speed from accelerometer jiggle in aquatic environments. *J. Exp. Biol.* **221**, jeb170449. doi:10.1242/jeb.170449

Capuano, F., Coppola, G., Randez, L. and de Luca, L. (2017). Explicit Runge-Kutta schemes for incompressible flow with improved energy-conservation properties. *J. Comput. Phys.* **328**, 86-94. doi:10.1016/j.jcp.2016.10.040

Charnyi, S., Heister, T., Olshanskii, M. A. and Rebholz, L. G. (2017). On conservation laws of Navier- Stokes Galerkin discretizations. *J. Comput. Phys.* **337**, 289-308. doi:10.1016/j.jcp.2017.02.039

Choi, H. and Moin, P. (2012). Grid-point requirements for large eddy simulation: Chapman's estimates revisited. *Phys. Fluids* **24**, 011702. doi:10.1063/1.3676783

Cressey, R. F. and Lachner, E. (1970). The parasitic copepod diet and life history of diskfishes (Echeneidae). *Copeia* **1970**, 310-318. doi:10.2307/1441652

Douglas, A. and Calambokidis, J. (2001). Regional and temporal patterns of remora occurrence on blue whales in the eastern Pacific Ocean. In Fourteenth Biennial Conference on the Biology of Marine Mammals. Vancouver, British Columbia.

Fertl, D. and Landry, A. (1999). Sharksucker (*Echeneis naucrates*) on a bottlenose dolphin (*Tursiops truncatus*) and a review of other cetacean-remora associations. *Mar. Mammal Sci.* **15**, 859-863. doi:10.1111/j.1748-7692.1999.tb00849.x

Flammang, B. E. and Kenaley, C. (2017). Remora cranial vein morphology and its functional implications for attachment. *Sci. Rep.* **7**, 5914. doi:10.1038/s41598-017-06429-z

Fulcher, B. A. and Motta, P. J. (2006). Suction disk performance of echeneid fishes. *Can. J. Zool.* **84**, 42-50. doi:10.1139/z05-167

Gamel, K. M., Garner, A. M. and Flammang, B. E. (2019). Bioinspired remora adhesive disc offers insight into evolution. *Bioinspir. Biomim.* **14**, 056014. doi:10.1088/1748-3190/ab3895

Goldbogen, J. A., Cade, D. E., Boersma, A. T., Calambokidis, J., Kahane-Rapport, S. R., Segre, P. S., Stimpert, A. K. and Friedlaender, A. S. (2017). Using digital tags with integrated video and inertial sensors to study moving morphology and associated function in large aquatic vertebrates. *Anat. Rec.* **300**, 1935-1941. doi:10.1002/ar.23650

Gough, W. T., Segre, P. S., Bierlich, K. C., Cade, D. E., Potvin, J., Fish, F. E., Dale, J., di Clemente, J., Friedlaender, A. S. and Johnston, D. W. (2019). Scaling of swimming performance in baleen whales. *J. Exp. Biol.* **222**, jeb204172. doi:10.1242/jeb.204172

Gudger, E. W. (1919). On the use of the sucking-fish for catching fish and turtles: studies in *Echeneis* or *Remora*, III. *Am. Nat.* **53**, 515-525. doi:10.1086/279729

Hoerner, S. F. (1965). *Fluid Dynamic Drag*. New Jersey: Hoerner Fluid Dynamics.

Hunt, J. C. R., Wray, A. and Moin, P. (1988). *Eddies, stream, and convergence zones in turbulent flows*. Technical Reports CTR-S88, Center for Turbulence Research, Stanford University.

Jayne, B. C. and Lauder, G. V. (1996). New data on axial locomotion in fishes: how speed affects diversity of kinematics and motor patterns. *Am. Zool.* **36**, 642-655. doi:10.1093/icb/36.6.642

Johnson, M. P. and Tyack, P. L. (2003). A digital acoustic recording tag for measuring the response of wild marine mammals to sound. *IEEE J. Ocean. Eng.* **28**, 3-12. doi:10.1109/JOE.2002.808212

Joubert, P. N. (2004). *Some aspects of submarine design, Part 1. Hydrodynamics*. Australian Government Department of Defence Report DSTO-TR-1622.

Kenaley, C. P., Stote, A., Ludt, W. B. and Chakrabarty, P. (2019). Comparative functional and phylogenomic analyses of host association in the remoras (Echeneidae), a family of hitchhiking fishes. *Integr. Org. Biol.* **1**, obz007. doi:10.1093/iob/obz007

Larsson, J., Kawai, S., Bodart, J. and Bermejo-Moreno, I. (2016). Large eddy simulation with modeled wall-stress: recent progress and future directions. *Mech. Eng. Rev.* **3**, 15-00418. doi:10.1299/mer.15-00418

Lauder, G. V. (2006). Locomotion. In *The Physiology of Fishes*, 3rd edn (ed. D. H. Evans and J. B. Claiborne), pp. 3-46. Boca Raton: CRC Press.

Lehmkuhl, O., Houzeaux, G., Owen, H., Chrysokentis, G. and Rodrigeuz, I. (2019). A low-dissipation finite element scheme for scale resolving simulations of turbulent flows. *J. Comput. Phys.* **390**, 51-65. doi:10.1016/j.jcp.2019.04.004

Lieske, E. and Myers, R. (1994). *Collins Pocket Guide. Coral reef fishes. Indo-Pacific & Caribbean including the Red Sea*. Collins.

Lighthill, M. (1971). Large-amplitude elongated-body theory of fish locomotion. *Proc. R. Soc. B* **179**, 125-138. doi:10.1098/rspb.1971.0085

Muir, B. S., Buckley, R. M. and Muim, B. S. (1967). Gill ventilation in *Remora remora*. *Copeia* **1967**, 581-586. doi:10.2307/1442235

O'Toole, B. (2002). Phylogeny of the species of the superfamily Echeneoidea (Perciformes: Carangoidei: Echeneidae, Rachycentridae, and Coryphaenidae), with an interpretation of echeneid hitchhiking behaviour. *Can. J. Zool.* **80**, 596-623. doi:10.1139/z02-031

Owen, H., Chrysokentis, G., Avila, M., Mira, D., Houzeaux, G., Borrel, R., Cajas, J. C. and Lehmkuhl, O. (2019). Wall-modeled large-eddy simulation in a finite element framework. *Int. J. Numer. Methods Fluids* **92**, 20-37. doi:10.1002/fld.4770

Piomelli, U. (2008). Wall-layer models for large-eddy simulations. *Prog. Aerosp. Sci* **44**, 437-446. doi:10.1016/j.paerosci.2008.06.001

Piomelli, U. and Balaras, E. (2002). Wall-layer models for large-eddy simulations. *Annu. Rev. Fluid Mech.* **34**, 349-374. doi:10.1146/annurev.fluid.34.082901.144919

Reichardt, H. (1951). Vollständige darstellung der turbulenten geschwindigkeitsverteilung in glatten leitungen. *Z. Angew. Math. Mech.* **31**, 208-219. doi:10.1002/zamm.19510310704

Sazima, I. (2018). Tenacious underwater fishers: Double-crested Cormorants, *Nannopterum auritus* (Suliformes: Phalacrocoracidae) dislodge and prey on suckerfish attached to a whale shark in Mexico. *Atual. Ornitológicas* **201**, 21-23.

Schlichting, H. and Gersten, K. (2000). *Boundary Layer Theory*, 8th edn, p. 422. New York: Springer.

Shur, M., Spalart, P. R., Strelets, M. K. and Travin, A. K. (2008). A hybrid rans-les approach with delayed-des and wall-modelled les capabilities. *Int. J. Heat Fluid Flow* **29**, 1638-1649. doi:10.1016/j.ijheatfluidflow.2008.07.001

Silva-Jr, J. M. and Sazima, I. (2003). Whalesuckers and a spinner dolphin bonded for weeks: does host fidelity pay off? *Biota Neotrop.* **3**, 1-5. doi:10.1590/s1676-06032003000200012

Steffensen, J. F. and Lomholt, J. P. (1983). Energetic cost of active branchial ventilation in the sharksucker, *Echeneis naucrates*. *J. Exp. Biol.* **103**, 185-192.

Strasburg, D. W. (1962). Some aspects of the feeding behavior of *Remora remora*. *Pac. Sci.* **16**, 202-206.

Trias, F. X. and Lehmkuhl, O. (2011). A self-adaptive strategy for the time integration of Navier-Stokes equations. *Numer. Heat Transfer B* **60**, 116-134. doi:10.1080/10407790.2011.594398

Vázquez, M., Houzeaux, G., Koric, S., Artigues, A., Aguado-Sierra, J., Arís, R., Mira, D., Calmet, H., Cucchietti, F., Owen, H. et al. (2016). Alya: multiphysics engineering simulation toward exascale. *J. Comput. Sci.* **14**, 15-27. doi:10.1016/j.jocs.2015.12.007

Vreman, A. W. (2004). An eddy-viscosity subgrid-scale model for turbulent shear flow: algebraic theory and applications. *Phys. Fluids* **16**, 3670-3681. doi:10.1063/1.1785131

Wang, T., Keller, F. J. and Zhou, D. (1996). Flow and thermal structures in a transitional boundary layer. *Exp. Therm. Fluid Sci.* **12**, 352-363. doi:10.1016/0894-1777(95)00126-3

Weihs, D., Fish, F. E. and Nicastro, A. J. (2007). Mechanics of remora removal by dolphin spinning. *Mar. Mammal Sci* **23**, 707-714. doi:10.1111/j.1748-7692.2007.00131.x

Yang, X. I. A., Park, G. I. and Moin, P. (2017). Log-layer mismatch and modeling of the fluctuating wall stress in wall-modeled large-eddy simulations. *Phys. Rev. Fluids* **2**, 104601. doi:10.1103/PhysRevFluids.2.104601